Received: 18 December 2024 | Revised: 29 January 2025 | Accepted: 3 February 2025

DOI: 10.1002/pro.70068

RESEARCH ARTICLE

THE PROTEIN SOCIETY WILEY

Unraveling the molecular grammar and the structural transitions underlying the fibrillation of a viral fibrillogenic domain

Frank Gondelaud[1] | **Julien Leval**[1] | **Lisha Arora**[2] | **Anuja Walimbe**[2] | **Christophe Bignon**[1] | **Denis Ptchelkine**[1] | **Stefania Brocca**[3] | **Samrat Mukhopadyay**[2] | **Sonia Longhi**[1]

[1]Laboratoire Architecture et Fonction des Macromolécules Biologiques (AFMB), UMR 7257, Aix-Marseille University and Centre National de la Recherche Scientifique (CNRS), Marseille, France

[2]Centre for Protein Science, Design and Engineering, Department of Chemical Sciences, and Department of Biological Sciences, Indian Institute of Science Education and Research (IISER) Mohali, Mohali, Punjab, India

[3]Department of Biotechnology and Biosciences, University of Milano-Bicocca, Milan, Italy

Correspondence
Sonia Longhi, Laboratoire Architecture et Fonction des Macromolécules Biologiques (AFMB), UMR 7257, Aix-Marseille University and Centre National de la Recherche Scientifique (CNRS), 163, Avenue de Luminy, 13288 Marseille CEDEX 09, France.
Email: sonia.longhi@univ-amu.fr

Funding information
Indo-French Centre for the Promotion of Advanced Research, Grant/Award Number: 6903-3; Agence Nationale de la Recherche, Grant/Award Number: ANR-21-CE11-0012-01; French Infrastructure for Integrated Structural Biology, Grant/Award Number: ANR-10-INSB-0005; Fondation pour la Recherche Médicale (FRM), Grant/Award Number: MND202310017898

Review Editor: Jean Baum

Abstract

Hendra virus (HeV) is a biosafety level 4 human pathogen belonging to the *Henipavirus* genus within the *Paramyxoviridae* family. In HeV, the phosphoprotein-encoding gene also drives the synthesis of the V and W proteins that are two major players in the host innate immune response evasion. These three proteins share a common intrinsically disordered N-terminal domain (NTD) and have distinct C-terminal domains. We recently reported the ability of a short region (i.e., PNT3), located within the shared NTD, to form fibrils. We subsequently identified a PNT3 motif (EYYY) critically involved in fibrillation and deciphered the contribution of each tyrosine to the process. Herein, we combined mutational studies with various biochemical and biophysical approaches to further investigate the molecular mechanisms underlying PNT3 fibrillation. The results show that (i) lysine residues play a critical role in driving fibrillation, (ii) hydrophobic residues affect the nucleation step, and (iii) charge distribution strongly affects the fibrillation propensities. Vibrational Raman spectroscopy data further validated the role of lysine residues in promoting fibrillation and enabled documenting the formation of cross-β amyloid structures. Altogether, these results illuminate the molecular mechanisms involved in fibril formation and pave the way towards the rational design of inhibitors.

KEYWORDS
amyloid-like fibrils, circular dichroism, disorder-to-order transitions, Hendra virus, intrinsically disordered proteins, negative staining transmission electron microscopy, paramyxoviruses, Raman spectroscopy, small-angle X-ray scattering, thioflavin T binding assays

1 | INTRODUCTION

Hendra virus (HeV) is a member of the *Henipavirus* genus within the *Paramyxoviridae* family (Eaton et al., 2007). Henipaviruses are zoonotic Biosafety Level 4 (BSL-4) pathogens that cause severe respiratory and neurological disease (Eaton et al., 2007). HeV is an enveloped virus with a non-segmented single-stranded RNA genome of negative polarity (Eaton et al., 2006). Its genome is encapsidated by an array of

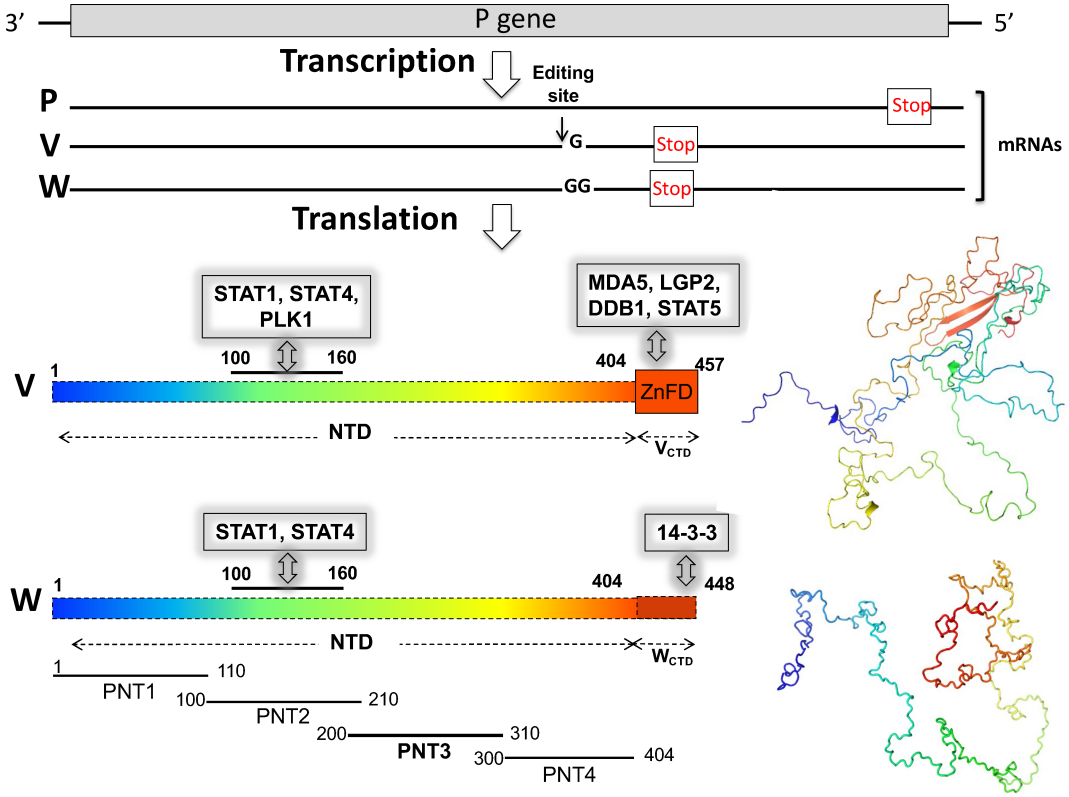

FIGURE 1 Scheme illustrating how the P gene drives the synthesis of the P, V, and W proteins, and modular organization of the HeV V and W proteins consisting of a common N-terminal domain (NTD) and of a distinct C-terminal domain (CTD). The shaded gray boxes indicate the interaction sites with human innate immune response proteins. The CTD of the V protein adopting a zinc-finger conformation is shown as a large box to emphasize that it is structured, in contrast to the NTD and CTD of the W protein. The various overlapping fragments within the NTD, as described in Salladini et al. (2021), are shown, with PNT3 in bold. For both the V and W proteins, a representative conformer, selected from the corresponding conformation ensemble (PED entry codes: 00182 and 00204 for HeV V (Salladini et al., 2021) and HeV W (Pesce et al., 2022), respectively), is shown. The conformers are shown in rainbow with blue and red colors corresponding to the N- and C-terminal ends, respectively.

nucleoprotein (N) monomers to yield a helical nucleocapsid that serves as a template for both viral transcription and replication. Synthesis of viral messengers and viral genome and antigenome is carried out by the polymerase complex made of the large protein (L), which bears all enzymatic activities, and the phosphoprotein (P), that tethers L onto the nucleocapsid template and maintains it in a soluble and active form (Abdella et al., 2020; Bloyet et al., 2016, 2019).

The N and P proteins of HeV and of the cognate Nipah virus (NiV) possess long intrinsically disordered regions (IDRs) (Gondelaud et al., 2022). While the N protein consists of a large structured domain (N_{CORE}) (Ker et al., 2021) followed by a C-terminal disordered region (N_{TAIL}) (Blocquel et al., 2012; Communie et al., 2013; Habchi et al., 2010, 2011; Martinho et al., 2013), the P protein consists of a long N-terminal intrinsically disordered domain (NTD) and a C-terminal region encompassing both structured and disordered regions (Beltrandi et al., 2015; Blocquel et al., 2013; Bruhn-Johannsen et al., 2014; Communie et al., 2013; Habchi et al., 2010, 2011; Jensen et al., 2020; Schiavina et al., 2020).

As is the case in many paramyxoviruses (Douglas et al., 2021), the P gene from HeV and NiV also encodes the C, V, and W proteins. While C is encoded by an alternative reading frame of the P gene, the V and W proteins result from a mechanism of co-transcriptional editing of the P mRNA. Specifically, while the addition of one non-templated guanosine at the editing site of the P messenger yields the V protein, the addition of two guanosines leads to the synthesis of the W protein (Figure 1).

Because the editing site is located at the end of the P gene region encoding NTD (Figure 1), P, V, and W share a common NTD and have distinct C-terminal domains (CTDs). While the CTD of W is disordered (Pesce et al., 2024), the CTD of V adopts a zinc-finger conformation (Salladini et al., 2017) (Figure 1). The V and W proteins play a key role in counteracting the antiviral type I interferon (IFN-I)-mediated response, and they do so by binding to a number of key cellular proteins involved in the antiviral response (Audsley & Moseley, 2013; Fontana et al., 2008; Tsimbalyuk et al., 2020) (Figure 1).

We previously reported the ability of a region within the HeV NTD (i.e., PNT3, aa 200–310) (Figure 1) to form fibrils (Salladini et al., 2021) and subsequently showed that this ability is also retained, although to a lesser extent, by the corresponding region of NiV (aa 200–314) (Nilsson et al., 2022). Interestingly, Congo red staining experiments provided hints that these fibrils form not only in vitro, but also in transfected or infected cells (Salladini et al., 2021), suggesting a probable functional role. Considering the critical role of the *Henipavirus* V and W proteins in evading the host innate immune response, we previously hypothesized that in infected cells PNT3-mediated fibrillar aggregates could sequester key cellular proteins involved in the antiviral response (Gondelaud et al., 2022). Consistent with the occurrence of the PNT3 region also within the *Henipavirus* W proteins, the latter were found to be able to fibrillate as well (Gondelaud et al., 2024; Pesce et al., 2022).

Within PNT3, an amyloidogenic motif encompassing three contiguous tyrosines (EYYY) was identified (Salladini et al., 2021). Substitution of three contiguous tyrosine residues with three alanine residues yielded a variant (referred to as PNT3^{3A}) that displayed dramatically reduced, though not abolished, fibrillation abilities (Salladini et al., 2021). Subsequent studies targeting each of the three individual tyrosines of the EYYY motif showed that the removal of a single tyrosine significantly decreased the ability to form fibrils independently of position, mainly affecting the elongation phase (Nilsson et al., 2022). In addition, these studies revealed that the C-terminal half of PNT3 acts as a natural dampener of fibrillation (Nilsson et al., 2022).

Here, in order to decipher the molecular grammar of PNT3 fibrillation, we designed and characterized a set of additional HeV PNT3 variants that were conceived to investigate the role of arginine and lysine residues, the impact of varying hydrophobicity, and the distribution of oppositely charged residues along the sequence. In addition, since previous studies failed to reveal a possible structural transition occurring during the fibrillation process, we used Raman spectroscopy to fill this gap. Results, as obtained by combining various biophysical and structural approaches, showed that lysine residues are the main drivers of PNT3 fibrillation, whereas aliphatic residues are mainly responsible for fibril nucleation. Modifying the distribution of opposite charges towards a more homogeneous distribution strongly promotes fibrillation. Finally, Raman spectroscopy studies provided insights into the structural organization of mature fibrils.

2 | RESULTS AND DISCUSSION

2.1 | Rational design, bioinformatics analysis, and generation of PNT3 variants

To thoroughly investigate the molecular determinants that control the fibrillogenic behavior of PNT3, we conceived an experimental design that addresses three parameters: the relative contribution of arginine and lysine residues, the overall hydrophobicity of the molecule, and the distribution of oppositely charged residues along the sequence. This approach relied on extensive targeted mutagenesis to systematically modify specific residues within either the full-length PNT3 protein or its truncated version (PNT3tr) devoid of the C-terminal half of the PNT3 sequence and previously shown to be more fibrillogenic (Nilsson et al., 2022).

PNTtr K_R variants. Our previous studies highlighted the critical role of tyrosine residues in PNT3 fibrillation (Nilsson et al., 2022; Salladini et al., 2021). Tyrosine residues are well known for their ability to establish cation–π interactions with basic residues (Gallivan & Dougherty, 1999). Here, to disentangle the relative contribution of arginine and lysine residues to these interactions, we replaced either all arginine residues with lysines (yielding the R^{all}K variant) or all lysines with arginines (yielding the K^{all}R variant) in the context of the more fibrillogenic PNT3 truncated variant (PNT3tr) (Figure 2a).

PNTtr hydrophobicity variants. As hydrophobic interfaces can drive fibril formation (for e,g, see Maltseva et al., 2023), we either increased or decreased the hydrophobicity of the PNT3tr sequence. To this end, we either replaced all four glycine residues with valine residues (to yield the G^{all}V variant) or replaced all valine (Eaton et al., 2006), isoleucine (Bloyet et al., 2016), and leucine (Bloyet et al., 2016) residues with glycine residues (to yield the VIL^{all}G variant) (Figure 2a).

PNT3 κ-values variants. Building on our previous work highlighting the role of electrostatics in PNT3 fibrillation (Nilsson et al., 2022), we further explored the influence of charged residues on the fibrillation process. In particular, we focused on charge patterning, a sequence property formalized through the normalized κ parameter and known to affect both the conformation of intrinsically disordered proteins (IDPs) (Bianchi et al., 2022; Das & Pappu, 2013; Tedeschi et al., 2018) and their condensation propensity (Bianchi et al., 2024; Nott et al., 2015; Pak et al., 2016; Schuster et al., 2020). To this end, we generated two variants with either evenly distributed (low-κ variant) or maximally clustered (high-κ variant) opposite charges. Non-charged residues were kept unchanged and only charged residues were permutated (Figure 2b), as previously described (Bianchi et al., 2022, 2024; Tedeschi et al., 2018). We did this in the context of the full-length PNT3 variant to obtain the lowest and the highest possible values of κ. Indeed, the fraction of charged residues (FCR) (0.36 for PNT3 and 0.28 for PNT3tr) dictates the highest κ value achievable for a given sequence. Starting with a κ value of 0.241 for *wt* PNT3, sequence permutations resulted in κ values as high as 0.461 and as low as 0.102, representing respectively

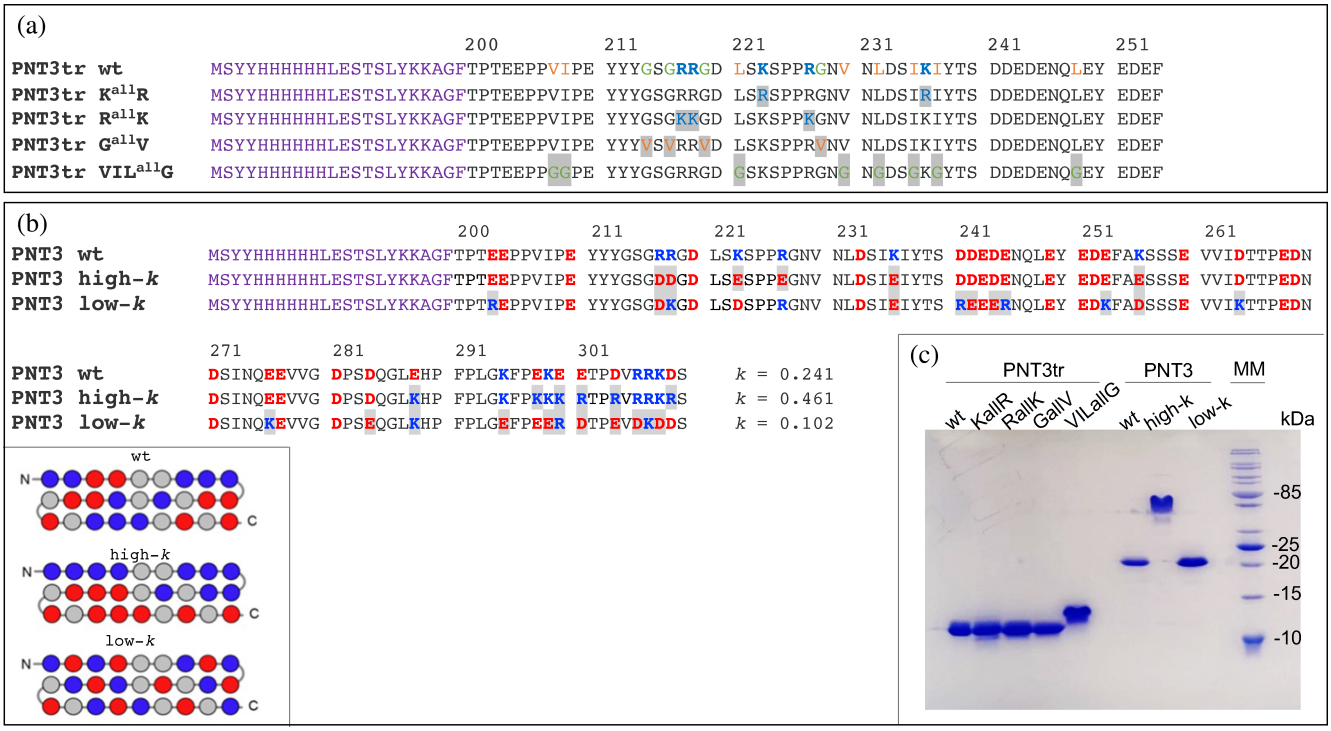

FIGURE 2 Amino acid sequences of truncated (a) and full-length (b) PNT3 variants expressed in *E. coli*. (a) Amino acid sequences of truncated PNT3 variants (PNT3tr) with vector-encoded N-terminal residues in violet, hydrophobic (non-aromatic) residues in orange, glycine in green, and lysine and arginine residues in blue. For each variant, the introduced substitutions are shown with a gray background. (b) Amino acid sequences of full-length variants with vector-encoded N-terminal residues in violet, acidic residues in red and basic residues in blue. Introduced substitutions are shown with a gray background. The corresponding κ values are also shown. The inset shows a schematic representation of the sequence of a set of proteins derived from a generic wild-type protein. Sequence variants are generated by either distributing oppositely charged residues more evenly (low-κ variant) or clustering them into two blocks at the N- and C-moieties (high-κ variant). Only charged residues were permutated, while the positions of non-charged residues were maintained. Blue and red spheres indicate positively and negatively charged residues, respectively, while gray spheres indicate all other amino acids. In panels A and B, amino acid numbering corresponds to the positions within the P/V/W proteins. (c) SDS–PAGE analysis of the final purified variants obtained after IMAC and SEC.

the maximum and minimum theoretical κ values for this sequence. These two variants can be considered as bona fide low- and high-κ variants: indeed, for proteins with an FCR > 0.2, κ values <0.12 and ≥0.25 are considered as "low" and "high", respectively (Holehouse et al., 2017).

All variants were analyzed in terms of their predicted disorder (Figure S1) and propensity to form amyloid-like fibrils (Figure S2) using the MeDor (Lieutaud et al., 2008) and FoldAmyloid (Garbuzynskiy et al., 2010) servers, respectively. MeDor analysis showed that the introduced substitutions have a moderate (if any) impact on the disorder content, with the notable exception of the PNT3tr $G^{all}V$ variant, which is less disordered (Figure S1), as expected based on its enriched content in hydrophobic residues. The latter is also the variant with the highest predicted amyloidogenicity (Figure S2): notably, in this case the amyloidogenic region encompassing the PEYYY motif is six residues longer. The variant with the least propensity to fibrillate is PNT3tr $VIL^{all}G$. Noteworthy, its PEYYY motif is no longer predicted to be an amyloidogenic region (Figure S2). PNT3tr $K^{all}R$ stands aside as it possesses an additional predicted amyloidogenic region (i.e., SIRIYT) (Figure S2). Of note, the three full-length PNT3 variants have the same predicted amyloidogenicity, indicating that the predictor is not sensitive to variations in charge distribution (Figure S2). Finally, and surprisingly, an amyloidogenic motif is predicted within the vector-encoded stretch encompassing the hexahistidine tag. Although this latter finding might raise concerns, it should be emphasized that the present study was designed to compare a set of variants that are endowed with different sequence properties while being all histidine-tagged. Thus, the impact of the hexahistidine tag (if any) is presumably the same for all of them, thereby enabling meaningful comparisons among variants. In addition, it should be noted that the pDEST17 vector is a commonly used bacterial expression vector that has not been reported to drive non-physiological fibrillation of recombinant proteins.

Besides, since fibrils may in principle results from a "maturation" process of droplets resulting from liquid–liquid phase separation (LLPS) we also analyzed the propensities of the variants to undergo LLPS using the MolPhase predictor (Liang et al., 2024) (Figure S3).

Indeed, we previously showed that PNT3 is predicted as a phase-separating protein (Salladini et al., 2021). Although PNT3 was found to phase-separate in the presence of a crowding agent, it should be noted that, so far, no evidence in support of a droplet state preceding the formation of fibrils was obtained, and FRAP analyses showed that PNT3 condensates have a solid-like nature (Salladini et al., 2021). The variant with the highest predicted LLPS score is PNT3tr VILallG, followed by PNT3 high-κ and PNT3tr KallR, whereas the variant with the least predicted phase-separating score is PNT3 low-κ. The predicted LLPS scores of the PNT3 high-κ and PNT3 low-κ variants are surprising, as the opposite trend would have been expected in light of the established correlation between extended conformations (expected and confirmed in PNT3 low-κ, see below) and enhanced LLPS (Garaizar et al., 2020).

All proteins were expressed in *Escherichia coli* as hexahistidine-tagged forms. They were purified from the total fraction of the bacterial lysate under denaturing conditions using immobilized metal affinity chromatography (IMAC) followed by size exclusion chromatography (SEC). The purity of the final purified products was assessed by SDS–PAGE (Figure 2c). Notably, the PNT3tr VIL^{all}G and PNT3 high-κ variants exhibit altered electrophoretic mobilities (Figure 2c). As previously reported, IDPs not only often exhibit intrinsically abnormal electrophoretic behavior compared to globular proteins, but are also particularly sensitive to even moderate changes in their composition/sequence, which can significantly alter their mobility (see (Bianchi et al., 2022; Das & Pappu, 2013; Schramm et al., 2019; Tedeschi et al., 2018) and references cited therein). The slower electrophoretic mobility of PNT3tr VIL^{all}G, which is deprived of hydrophobic residues, can be attributed to its higher disorder content and diminished affinity towards the SDS alkyl moiety. The slower migration of the PNT3 high-κ variant, in which opposite charges are clustered, is due to reduced interaction with the anionic SDS headgroup, probably because of steric hindrance presumably arising from a collapsed protein conformation (Das & Pappu, 2013). This finding mirrors previous observations on unrelated IDPs (Tedeschi et al., 2018). Note that the identities of all variants were confirmed by mass spectrometry (MS) analysis of proteolytic peptides (Figure S4).

2.2 | Impact of basic and aliphatic residues on the conformational and fibrillation properties of PNT3 truncated variants

We first used SEC to investigate the hydrodynamic properties of truncated variants (Table 1). For each variant, we determined the Stokes radius (R_S) and calculated the compaction index (CI). By comparing the experimentally observed Stokes radius (R_S^{Obs}) with the theoretical Stokes radii expected for the various conformational states, all proteins were found to have R_S values consistent with a pre-molten globule (PMG) state (Uversky, 2002) or with that expected for an IDP (Marsh & Forman-Kay, 2010). CIs of the truncated variants vary from 0.44 (PNT3tr R^{all}K, the most extended form) to 0.60 (VIL^{all}G, the most compact form). The high compactness of VIL^{all}G is puzzling, as the opposite behavior would be expected considering the well-established role of aliphatic residues in driving chain compaction. As previously observed (Nilsson et al., 2022), *wt* PNT3tr is comparatively more compact (CI = 0.53) than *wt* full-length PNT3 (CI = 0.36) (Table 1), consistent with a role of the second half of the protein in chain expansion. The results presented here suggest that the higher compactness of *wt* PNT3tr may not primarily arise from the hydrophobic nature of its VIL residues. Instead, the increase in compactness (from CI = 0.53 to 0.60) may be attributed to the reduction of steric hindrance following the replacement of VIL residues with glycine.

The increase in compactness observed in the K^{all}R variant (from CI = 0.53 to 0.58) and the decrease in the R^{all}K variant (from CI = 0.53 to 0.48), although slight, is consistent with the different roles of lysine and arginine in molecular interactions. Arginine contributes to intramolecular interactions more robustly than lysine due to its ability to form relatively stronger bonds that are less affected by the dielectric constant of the medium (Kumar et al., 2018).

To determine the impact of each substitution on fibrillation propensity, the truncated variants were incubated in urea-free buffer for 3 days, and then analyzed using turbidity and thioflavin T (ThT) fluorescence measurements, along with negative-staining electron microscopy (NS-EM) (Figure 3a–c). Far-UV circular dichroism (CD) spectroscopy experiments were also performed on both freshly prepared and incubated samples (Figure 3d). PNT3tr was found to be insoluble and yet to bind ThT, suggesting the possible formation of fibrils (Figure 3a,b). Indeed, fibrillar aggregates, though not very abundant, were observed in the micrographs (Figure 3c). Substituting lysine residues with arginine (PNT3tr K^{all}R) not only leads to a highly insoluble variant but also strongly reduces the fibrillation process, with extremely rare and very shorts fibrils being detectable by NS-EM (Figures 3a–c and S5a). Noteworthy, the opposite substitution (PNT3tr R^{all}K) enhances solubility and strongly promotes fibrillation (Figure 3a–c). These findings strongly disagree with the in silico analyses that predict the opposite behavior (Figure S2). Intriguingly, PNT3tr K^{all}R binds ThT (Figure 3b) despite its dramatically reduced ability to fibrillate. While ThT is considered an amyloid-specific dye that primarily binds amyloid fibrils due to their enrichment in β-sheet structure, it can also interact with

TABLE 1 Stokes radii (R_S^{Obs}, Å) of the PNT3tr variants inferred from the elution volume of the major SEC peak.

Proteins	Mass (Da)	R_S^{Obs}	R_S^{NF}	R_S^{PMG}	R_S^{U}	R_S^{IDP}	R_S^{Obs}/R_S^{NF}	R_S^{Obs}/R_S^{PMG}	R_S^{Obs}/R_S^{U}	R_S^{Obs}/R_S^{IDP}	CI
PNT3tr wt	9020	20.7	16.1	22.6	25.8	22.7	1.28	0.91	0.80	0.91	0.53
PNT3tr $K^{all}R$	9076	20.2	16.2	22.7	25.9	22.7	1.25	0.89	0.78	0.89	0.58
PNT3tr $R^{all}K$	8936	21.4	16.1	22.6	25.7	22.7	1.33	0.95	0.83	0.94	0.44
PNT3tr $VIL^{all}G$	8599	19.6	15.9	22.2	25.2	22.7	1.23	0.88	0.78	0.86	0.60
PNT3tr $G^{all}V$	9188	21.0	16.2	22.8	26.0	22.7	1.30	0.92	0.81	0.93	0.51

Note: The expected values for the natively folded (NF), pre-molten globule (PMG), unfolded (U), and disordered (IDP) states are presented, along with the ratios between the R_S^{Obs} and the R_S value expected for each state. Additionally, compaction index (CI) values are provided.

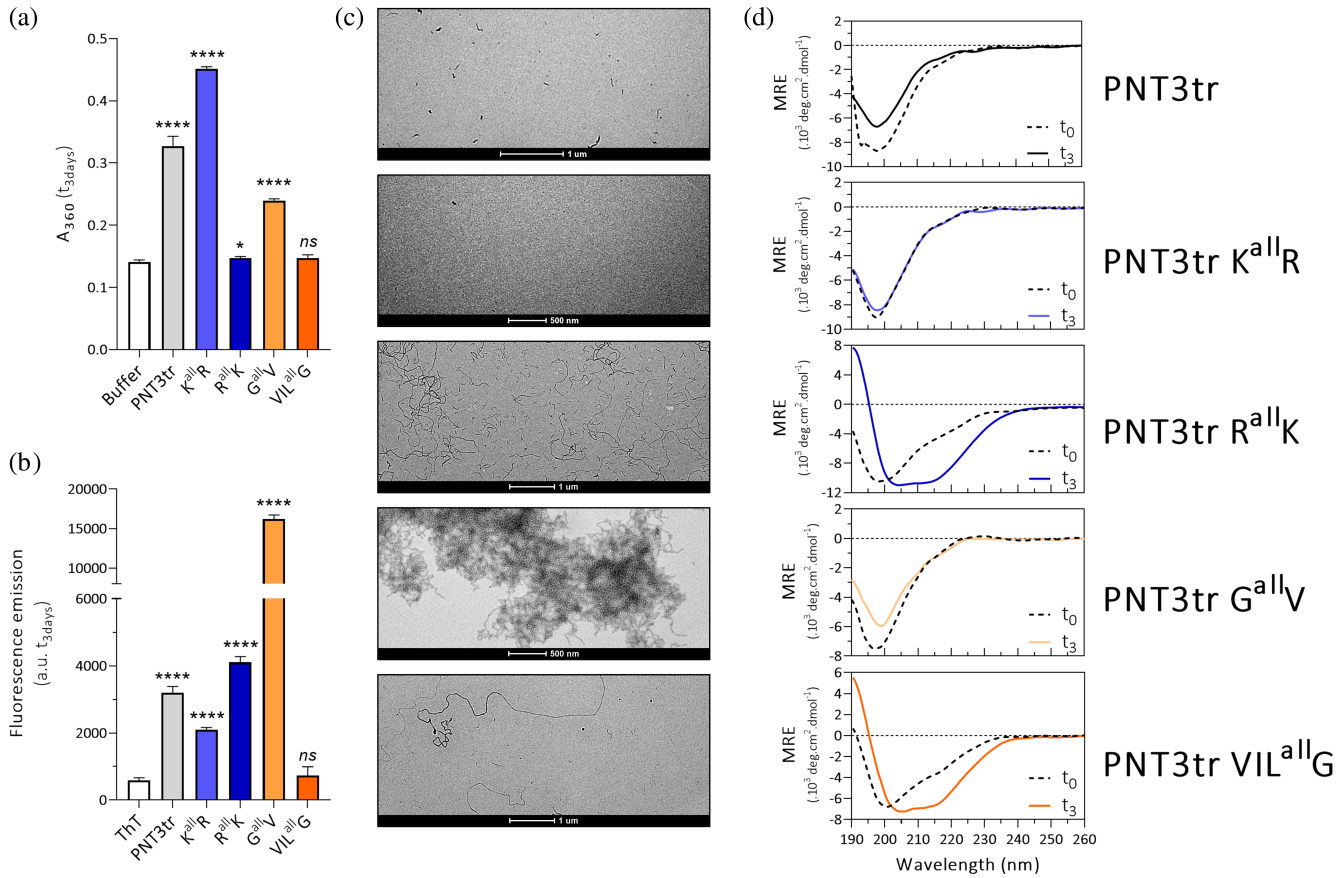

FIGURE 3 Role of basic and aliphatic residues in PNT3tr conformational properties and fibrillation. (a) Turbidity ($n = 4$) and (b) ThT fluorescence measurements ($n = 4$) of PNT3tr variants after 3 days of incubation. Asterisks indicate a statistically significant difference ($p < 0.0001$) compared to the control condition without protein; ns: not significant. (c) Micrographs of the same samples after 3 days of incubation. (d) Far-UV circular dichroism spectra of PNT3tr variants recorded immediately after urea removal (t_0) or after 3 days of incubation (t_3).

native proteins thereby leading to an increase in fluorescence intensity in the absence of fibrils, as well illustrated by acetyl-cholinesterase (Sulatskaya et al., 2018).

The formation of fibrils by the PNT3tr $R^{all}K$ variant is accompanied by the formation of secondary structures (15% α-helix, 29% β-strands, and 21% turns according to CD spectra deconvolution), while no such transition was observed for PNT3tr (that moderately fibrillates) or PNT3tr $K^{all}R$ (that does not fibrillate) (Figure 3d). These results highlight the major role of lysine residues in PNT3 solubility, formation of regular secondary structure elements, and fibrillation.

The most aliphatic variant, that is, PNT3tr $G^{all}V$, was found to be relatively insoluble (though surprisingly more soluble than the wt) but to strongly bind ThT (Figure 3a,b). In agreement with the predictions (Figure S2), the substitution of glycine with valine residues strongly promotes fibril formation, as indicated by the presence of a massive tangle of fibrillar aggregates observed by NS-EM (Figure 3c). However, in this case, fibril formation is not accompanied by detectable

secondary structure transitions (Figure 3d). Conversely, substitution of all aliphatic residues with glycine (PNT3tr VIL^{all}G) significantly increases the solubility of the variant (Figure 3a). Surprisingly, although PNT3tr VIL^{all}G does not significantly bind ThT (Figure 3b), long fibrils of several micrometers were observed in the corresponding micrographs (Figure 3c) and a disorder-to-β transition was observed by CD (6% α-helix, 34% β-strands, and 21% turns according to CD spectra deconvolution) (Figure 3d). The ability of this variant to form spectacularly long fibrils strongly contradicts predictions that identify it as the least amyloidogenic variant (Figure S2).

The poor binding of ThT by PNT3tr VIL^{all}G, which forms exceptionally long, though poorly abundant, fibrils, might stem from the fact that ThT fluorescence intensity reports more on nucleation than on fibril length, as already observed (Gondelaud et al., 2024). In addition, the lack of ThT fluorescence, despite the presence of fibrillar species, may also arise from specific fibril structural features. Indeed, both ThT binding efficacy and fluorescence intensity resulting from binding are not uniform across all amyloid fibrils, as well exemplified by FUS (Nomura et al., 2014) and the Japanese mutant of Aβ (Cloe et al., 2011), both of which form fibrils that poorly bind ThT.

Taken together, these observations suggest that aliphatic residues strongly promote fibril nucleation, with an increased number of fibrils at the cost of their length. Conversely, the loss of aliphatic residues does not abolish fibrillation and results in the formation of fewer but much longer fibrils (Figure 3c).

For the whole set of truncated variants, no correlation was found between turbidity and LLPS scores (Figure S3), suggesting that high turbidity values are unlikely to arise from bona fide phase separation processes, in line with the lack of experimental data to support a scenario of maturation of phase-separated droplets towards a fibrillar state.

Note that PNT3tr R^{all}K and VIL^{all}G, that is, the two variants undergoing structural changes upon incubation, exhibit some secondary structure even before the incubation process begins. This is evidenced by a weak negative absorption peak at around 215 nm (Figure 3d). This transiently populated β-structure likely primes the structural transition by lowering entropic cost. The absence of fibrils in non-incubated samples of these two variants (Figure S5a), combined with the gain of regular secondary structures upon incubation, supports the conclusion that the fibrillation process drives the structural transition. Intriguingly, fibrillation is not systematically accompanied by a detectable disorder-to-order transition. This is well illustrated by wt PNT3tr and, most importantly, by PNT3tr GallV, that is, the variant endowed with the highest fibrillogenic potential (see also Figure S5a, which shows that it strongly nucleates immediately after urea removal). It should be noted, however, that we cannot rule out the possibility that a structural transition may occur while escaping detection by CD.

To unravel the precise nature of the structural transition that occurs during the fibrillation process, we used Raman spectroscopy. Vibrational Raman spectroscopy is a label-free, non-invasive technique reporting on the structural characteristics of the polypeptide chain backbone in addition to the local environment surrounding the amino acid side chains (Maiti et al., 2004; Rygula et al., 2013; Tuma, 2005). Any change in the band positions and intensities of these vibrational bands indicates alterations in the secondary structure, hydrogen bonding patterns, and side chain interactions, providing valuable insights into the formation of amyloid assemblies (Avni et al., 2023; Devitt et al., 2019). We decided to focus on PNT3tr R^{all}K, that is, the variant with the highest fibrillation propensities and shown to undergo a disorder-to-order transition by CD. To evaluate the impact of substituting arginine with lysine residues, we concomitantly also examined the *wt* PNT3tr variant.

Raman spectroscopy analyses were carried out on the pellet obtained by centrifuging samples incubated at 37°C for either 1 (PNT3tr R^{all}K) or 3 days (PNT3tr), that is, under conditions where they form fibrils (Figure S5a). The rationale for the reduced incubation time of PNT3tr R^{all}K resides in its much higher fibrillogenicity compared to *wt* PNT3tr (Figure 3).

The vibrational spectra of *wt* PNT3tr and PNT3tr R^{all}K samples comprise various signature Raman bands, including Amide I (1600–1700 cm^{-1}) and Amide III (1230–1300 cm^{-1}) modes of bond vibrations, which were attributed primarily to the stretching of the carbonyl group (C═O) and a combination of in-plane stretching of C—N bonds and bending of N—H bonds within the polypeptide chain backbone, respectively (Figures 4a and S6a,b). The Raman spectra of the fibrillar aggregates formed by PNT3tr and PNT3tr R^{all}K exhibit an Amide I band centered at ~1670 cm^{-1}, indicating the presence of significant β-sheet conformations within these fibrillar aggregates (Figures 4b and S6c,d).

However, a closer look at the spectra of both variants revealed differences in the full width at half maximum (FWHM) values. While PNT3tr showed an FWHM of ~53 cm^{-1}, the fibrillar aggregates of PNT3tr R^{all}K displayed a reduced FWHM of ~44 cm^{-1}, suggesting a stronger β-sheet propensity originating from enhanced hydrogen bonding stabilizing the β-sheet-rich amyloid core of the PNT3tr R^{all}K variant. Next, we focused on Amide III, which appears as an intense, broad Raman band positioned at ~1232 cm^{-1} for both variants. To gain deeper insights into the conformational characteristics and secondary structure of these fibrillar aggregates, we performed spectral deconvolution of the Amide III region. For PNT3tr, this analysis revealed two broad overlapping peaks at ~1220 and ~1251 cm^{-1}, corresponding to β-sheets (~63.8%) and non-regular or disordered structural elements (~36.2%), respectively.

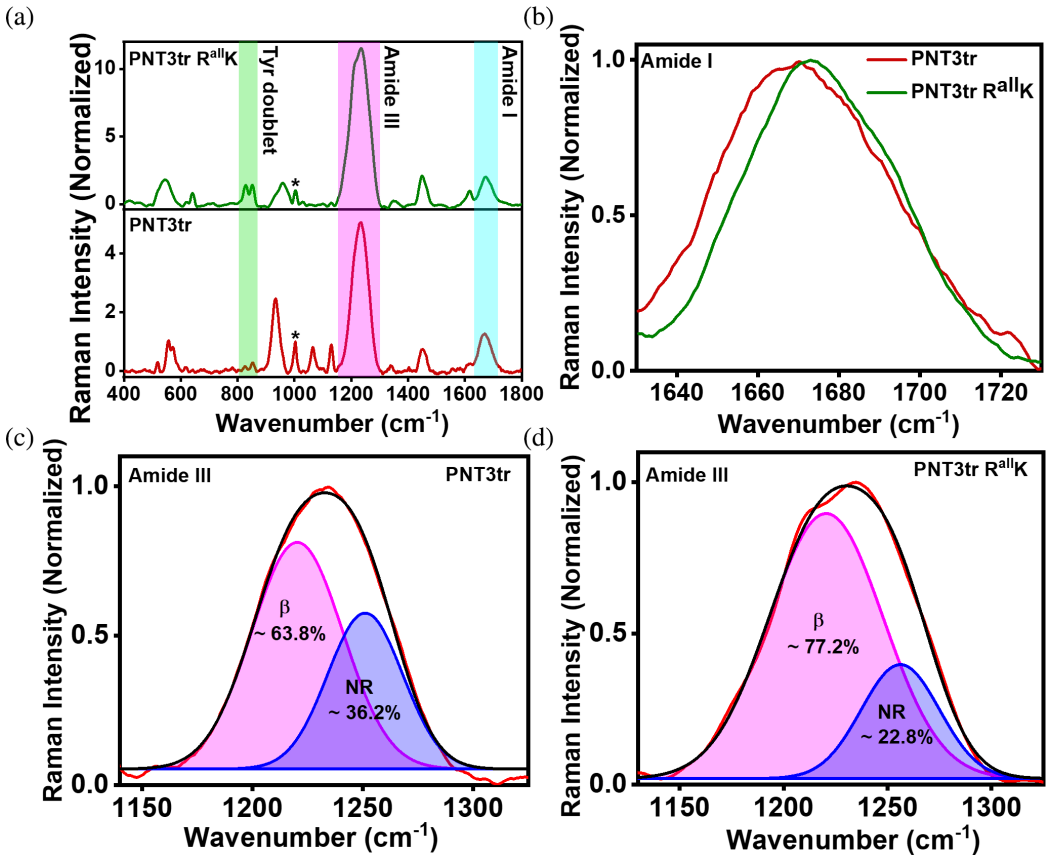

FIGURE 4 Vibrational Raman spectroscopy measurements of fibrils of both PNT3 variants. (a) Normalized vibrational Raman spectra obtained from the fibrils of PNT3tr (red) and PNT3tr R^{all}K (olive), in which relevant bands are highlighted. Data represent the mean of three independent samples. (b) Comparison of Amide I band of the two PNT3 variants, showing a relatively broader band for PNT3tr aggregates. Spectral deconvolution of the Amide III band obtained for fibrils of PNT3tr (c) and PNT3tr R^{all}K (d). The red and black lines represent the experimental and cumulative fits, respectively. The contribution of individual structural components (β-sheet: magenta; non-regular structures: blue) is shown as a percentage of the area under the curve.

However, the spectral deconvolution of the Amide III band for the PNT3tr R^{all}K variant showed a greater contribution of β-sheet architecture (~77.2%) and a reduced contribution of disordered structures (~22.8%) within these fibrillar aggregates, indicating enhanced fibrillation and compact amyloid structures (Figure 4c,d and Table S1). In addition to Amide I and Amide III, the Raman spectra also exhibit additional bands due to backbone deformations and different vibrational modes of aromatic amino acids. Specifically, the tyrosine Fermi doublet, which arises from the Fermi resonance between the fundamental ring-breathing planar vibration mode and the overtone of the non-planar ring-bending vibration of the phenolic ring in the tyrosine side chain, was also observed. The tyrosine doublet ratio exhibits extreme environmental sensitivity with respect to solvent hydrogen bonding, thus reporting on the surrounding hydrophobicity/hydrophilicity and solvent accessibility, and is estimated from the intensity ratio at 850 and 830 cm^{-1} wavenumbers (Hernández et al., 2015; Siamwiza et al., 1975). The ratio can range from 0.25 to 2, where increased values indicate reduced π–π stacking of the phenol rings corresponding to enhanced solvent exposure. The vibrational Raman spectra for the PNT3tr fibrillar aggregates provided an intensity ratio of ~1.72, suggesting a predominantly solvent-exposed and largely solvated phenol ring of the tyrosine residues. However, this ratio is significantly reduced for the fibrillar aggregates of PNT3tr R^{all}K, indicating a greater extent and stronger tendency for aromatic π–π stacking within the more ordered, cross-β fibrillar aggregates of this variant.

Taken together, our Raman measurements indicate a structural transition into an ordered amyloid-like state with enhanced fibrillogenicity for the PNT3tr R^{all}K variant, thus confirming and extending the results presented above.

2.3 | Impact of opposite charge distribution on the conformational and fibrillation properties of PNT3

We then analyzed the impact of varying the opposite charge distribution (κ variants) on both the structural

TABLE 2 Stokes radii (R_S^{Obs}, Å) of the PNT3 *κ*-values variants inferred from the elution volume of the major SEC peak.

Proteins	Mass (Da)	R_S^{Obs}	R_S^{NF}	R_S^{PMG}	R_S^{U}	R_S^{IDP}	R_S^{Obs}/R_S^{NF}	R_S^{Obs}/R_S^{PMG}	R_S^{Obs}/R_S^{U}	R_S^{Obs}/R_S^{IDP}	CI
PNT3 wt	15,198	**28.7**	19.4	27.9	33.9	30.0	1.48	1.03	0.85	0.96	0.36
PNT3 high-k	15,198	**27.7**	19.4	27.9	33.9	30.0	1.43	0.99	0.82	0.92	0.43
PNT3 low-k	15,198	**28.9**	19.4	27.9	33.9	30.0	1.48	1.03	0.85	0.96	0.35

Note: The expected values for the natively folded (NF), pre-molten globule (PMG), unfolded (U), and disordered (IDP) states are presented, along with the ratios between the R_S^{Obs} and the R_S value expected for each state. Additionally, compaction index (CI) values are provided.

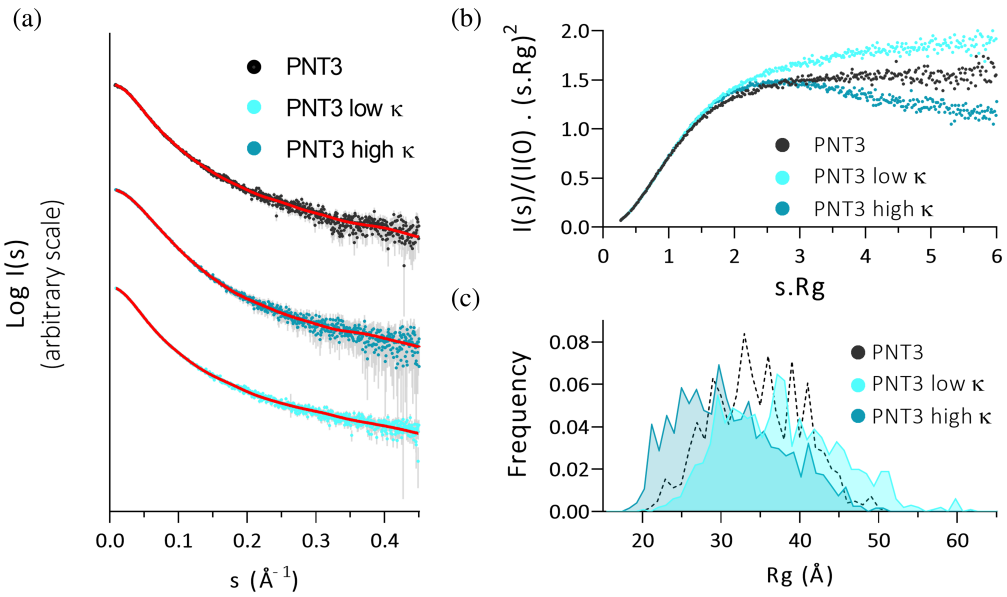

FIGURE 5 Impact of opposite charge distribution on the conformational properties of PNT3. (a) Scattering intensities of *wt* PNT3, PNT3 low-*κ*, and PNT3 high-*κ* obtained during SEC-SAXS experiments, accompanied by their respective EOM fits (red curves). (b) Corresponding normalized Kratky plots. (c) R_g distribution obtained after EOM deconvolution of the three proteins.

properties and fibrillogenic propensities of full-length PNT3. The hydrodynamic properties of PNT3 and PNT3 low-*κ* were found to be in the range of values expected for either a PMG state or for an IDP, whereas the high-*κ* variant is more compact and its measured R_S perfectly fits with the value expected for a PMG state (Table 2). The CIs of the low-*κ* and high-*κ* variants (0.35 and 0.43, respectively) reflect the well-documented compaction effect brought by opposite charge clustering (Bianchi et al., 2022; Das & Pappu, 2013; Tedeschi et al., 2018).

For this set of variants, which exhibit the most contrasting conformational properties out of all the variants studied herein, we further deepen the study of their structural properties using small-angle X-ray scattering coupled to SEC (SEC-SAXS) (Figure 5a). Although we previously reported SEC-SAXS studies of *wt* PNT3 (Salladini et al., 2021), this variant was herein investigated again under exactly the same conditions used for the other variants, thereby enabling meaningful comparisons.

For all PNT3 proteins, linearity of the Guinier region in the resulting scattering curves (Figure S7a) enabled reliable estimation of the radius of gyration (R_g) (Table 3). The observed R_g values are consistent with the expected degree of compaction of each variant: the low-*κ* variant exhibits the most extended structure, with an R_g value ($R_g \simeq 38$ Å) close to that expected for a chemically unfolded (U) conformation, whereas the high-*κ* variant shows the most compact conformation, with an R_g value ($R_g \simeq 31$ Å) typical of an IDP (Table 3).

Accordingly, the normalized Kratky plots point out a progressive increase in compactness from the low-*κ* variants to the *wt* and high-*κ* variants (Figure 5b). The scattering intensities were deconvoluted using EOM (Bernado et al., 2007; Tria et al., 2015) (Figures 5c and S7b). Consistent with the differences in the compactness of the variants, the R_g distributions are shifted towards lower or higher values for the high-*κ* and low-*κ* variants, respectively. Hence, both the hydrodynamic parameters and scattering intensities indicate a notable variation in the structural compactness among the *κ* variants of PNT3.

To assess how the conformational properties of *κ* variants impact their fibrillation propensity, these proteins were incubated for 7 days and subsequently analyzed in the same manner as the PNT3tr variants (Figures 6 and S5b). The rationale for this prolonged incubation time lies in the already established lower fibrillogenicity of full-length PNT3 compared to its truncated form (Nilsson et al., 2022). Both the low- and high-*κ* variants showed slightly reduced solubility compared to *wt* PNT3 (Figure 6a) and increased binding to

TABLE 3 R_g and D_{max} obtained from SEC-SAXS studies and expected values for the various conformational states.

Proteins	$I(0)$ (cm^{-1})	R_g (Å) (Guinier)	D_{max} (Å)	R_g^{IDP} (Å)	R_g^{U} (Å)	R_g^{NF} (Å)
PNT3 *wt*	19.57 ± 0.067	34.3 ± 0.30	142			
PNT3 high-k	22.08 ± 0.046	31.3 ± 0.10	120	32.6	35.9	15.2
PNT3 low-k	0.028 ± 7.2 × 10^{-5}	38.2 ± 0.21	152			

Abbreviations: D_{max}, maximal intramolecular distance from $P(r)$; $I(0)$, intensity at zero angle as determined from Guinier approximation; R_g^{IDP}, R_g expected for an IDP based on simple power law model; R_g^{NF}, theoretical R_g value expected for a natively folded (NF) protein; R_g^{U}, theoretical R_g value expected for a chemically denatured (U) protein; R_g Guinier, R_g values as obtained from Guinier approximation.

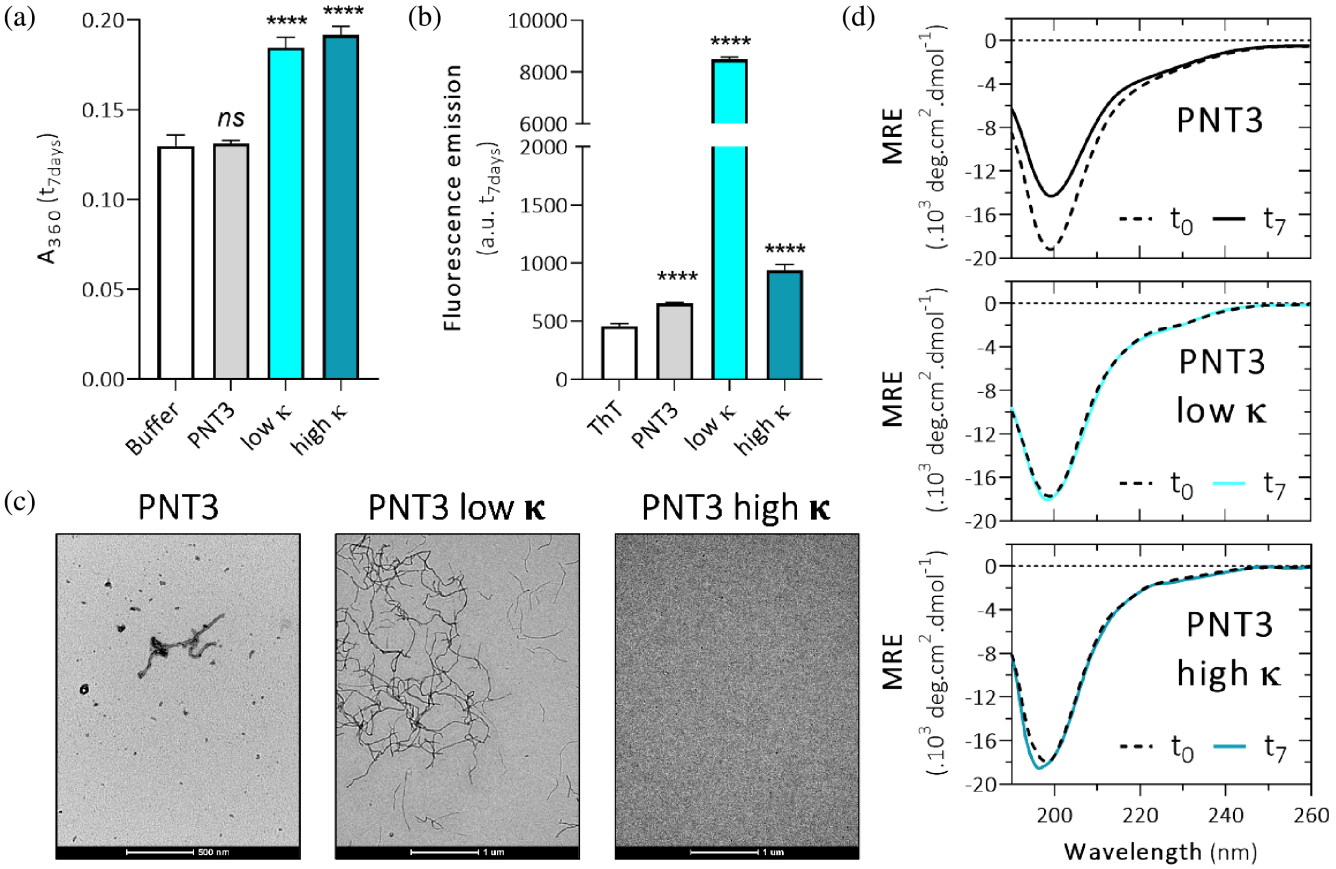

FIGURE 6 Impact of opposite charge distribution on PNT3 fibrillation propensity. Turbidity (a) and ThT fluorescence measurements (b) of PNT3, PNT3 low-*κ* and PNT3 high-*κ* after 7 days of incubation. Asterisks indicate a statistically significant difference ($p < 0.0001$) with respect to the control condition without protein; ns: not significant. (c) Micrographs of the same samples obtained after 7 days of incubation. (d) Far-UV CD spectra of PNT3 variants analyzed immediately after urea removal (t_0) or after 7 days of incubation (t_7).

ThT (Figure 6b). The low-*κ* variant demonstrated the highest ThT-binding ability (Figure 6b), which correlates with its pronounced fibrillogenicity, as confirmed by NS-EM (Figure 6c). In contrast, no fibrils were observed in the micrographs of the high-*κ* variant, despite its superior ThT binding capacity compared to PNT3 (Figure 6b,c). The inability of this variant to fibrillate despite its significant ThT-binding ability is reminiscent of the behavior of the PNT3tr K^{all}R variant discussed above and likely reflects unspecific binding to non-fibrillar species.

The inconsistencies between the ThT binding data and the TEM data observed for these two latter variants, as well as for the PNT3tr VIL^{all}G variant, challenge the extent to which ThT fluorescence can be used as a proxy for fibrillation. We would like to emphasize that ThT-binding assays should be systematically complemented by other analytical methods to draw definite conclusions about fibrillogenic potential.

The inability of the high-*κ* variant to fibrillate, coupled with the enhanced fibrillogenicity of the low-*κ* variant, suggests a critical role for lysine residues and their linear rearrangement, as also hinted by the behavior of the PNT3tr K-R variants. Since the total number of lysine residues remains constant among *κ*-variants, it is plausible that the observed differences in

fibrillogenic propensity among these variants arise from the distribution of lysines. In particular, the more evenly distributed lysine residues in the low-κ variant may contribute significantly to its fibrillation. The high fibrillation propensity of the low-κ variant, which has a highly extended conformation, together with the inability to fibrillate of the high-κ variant, supports an anticorrelation between the fibrillogenic potential and the compactness degree. Note that the predictions failed to capture this differential fibrillogenicity (Figure S2), thus illustrating the unparalleled power of the experimental studies.

Interestingly, and in striking contrast to the behavior of the truncated variants exhibiting the highest fibril elongation propensities (i.e., $R^{all}K$ and $VIL^{all}G$) (Figure 3d,e), fibrillation of the highly fibrillogenic low-κ variant does not involve any detectable secondary structure rearrangement, as indicated by the CD spectra recorded before and after 7 days of incubation (Figure 6d). However, possible structural transitions that escape detection cannot be excluded. Notably, a decrease in the signal intensity was observed in the spectrum of *wt* PNT3 upon incubation, which is in agreement with previous observations (Salladini et al., 2021).

Finally, as already noticed for the truncated variants, no coherent correlation was found between the turbidity and LLPS scores (Figure S3).

3 | CONCLUSIONS

In this study, we used the pro-amyloidogenic PNT3 fragment from the Hendra virus P/V/W proteins to dissect the molecular factors driving its fibrillation. We showed that hydrophobic residues play a crucial role in the fibrillation process, especially in the nucleation step, in line with their well-known role in driving protein aggregation. In addition, we showed that lysine residues play a critical role in promoting PNT3 fibrillation. Besides, our studies indicate that opposite charge clustering (high-κ variant) results in an increase in protein compactness, paralleled by a strong inhibition of fibrillation. Conversely, the PNT3 low-κ variant, which adopts a highly extended conformation, was the most fibrillogenic construct. This is consistent with a scenario where a strong tendency to establish intramolecular interactions counteracts the propensity to establish intermolecular interactions required for condensation and/or fibrillation processes, in line with previous reports (Bianchi et al., 2024; Garaizar et al., 2020; Nott et al., 2015; Pak et al., 2016; Schuster et al., 2020).

Interestingly, fibrillation does not systematically involve a disorder-to-order transition detectable by CD spectroscopy, as exemplified by PNT3tr $G^{all}V$ and PNT3 low-k, and, to a lesser extent, by wt PNT3tr and PNT3. This may reflect a moderate structural transition that can escape detection by CD. This is indeed the case for the PNT3tr variant, for which Raman spectroscopy, which is more sensitive to local structural changes than CD (Rygula et al., 2013), revealed the presence of a significant β-sheet content. The variability in the CD profiles of the incubated samples containing fibrils supports the conclusion that the fibrils formed by the set of variants herein studied do not constitute a structurally homogeneous group. In fact, some of these fibrils are conceivably characterized by an ordered core encompassing a very short protein segment, whose disorder-to-order transition escapes detection by CD. In line with this, Raman spectroscopy not only revealed the presence of a higher β-sheet content in the fibrils formed by the PNT3tr $R^{all}K$ variant compared to PNT3tr, but also enabled documenting solvent exposure of the phenol ring of tyrosine in PNT3tr fibrils, whereas PNT3tr $R^{all}K$ fibrils show stronger aromatic π–π stacking, supporting a more ordered cross-β structure. In the same vein, the lack of ThT fluorescence signal in the case of PNT3tr $VIL^{all}G$, along with the exceptionally long fibrils formed by this variant, hint at a possible different structural arrangement in these fibrils, providing further support for the structural heterogeneity of fibrils across variants.

In conclusion, the present study sheds light on the molecular grammar of PNT3 fibrillation and paves the way towards the rational design of fibrillation inhibitors.

4 | MATERIALS AND METHODS

4.1 | Bioinformatics analyses

Disorder predictions were obtained using a modified in-house version of the METaserver of DisORder MeDor (Lieutaud et al., 2008). MeDor allows fast, simultaneous analysis of a query sequence using multiple predictors. It provides a graphical interface with a unified view of the output of the multiple disorder predictors. MeDor includes the prediction of transmembrane regions (Phobius) and secondary structure prediction (SSP), based on the StrBioLib library of the Pred2ary program, Hydrophobic Cluster Analysis (HCA), DorA (an unpublished predictor developed in the AFMB lab that uses the size and abundance of hydrophobic clusters in the HCA plot to predict disorder), MoreRONN, FoldUnfold, FoldIndex, and MobiDB-lite. MobiDB-lite is a metapredictor that uses eight different disorder predictors (GlobPlot, three versions of ESpritz, two versions of IUPred, and two versions of DisEMBL) to derive a consensus that is refined to remove short disordered regions and retain only those that consist of at least 20 consecutive residues predicted as disordered. Beyond displaying the consensus prediction of MobiDB-lite (Consensus MobiDB), MeDor also

generates two consensus disorder predictions, one corresponding to regions predicted as disordered by the majority of predictors (Consensus1) and one corresponding to regions predicted as disordered by *all* the predictors (Consensus 2).

Amyloidogenic regions were predicted using the FoldAmyloid server (http://bioinfo.protres.ru/fold-amyloid/) (Garbuzynskiy et al., 2010) and default parameters. Predictions of the propensity to undergo LLPS were obtained using MolPhase predictor (http://molphase.sbs.ntu.edu.sg/) (Liang et al., 2024).

4.2 | Generation of the constructs

The DNA sequences encoding the different HeV PNT3 variants, optimized for *E. coli* expression, were synthetized from Genscript and supplied already inserted into a commercially available vector pUC57. Each gene was flanked by attB1 and attB2 sequences, thus enabling cloning using the Gateway® technology (Invitrogen, Carlsbad, CA, USA). The inserts were first amplified by PCR using attL1a and attL2a primers (Gruet et al., 2012) (Eurofins Genomics Germany GmbH, Ebersberg, Germany). After *Dpn*I treatment (New England Biolabs, Ipswich, MA, USA) to remove methylated DNA, the PCR product was purified and inserted into the pDEST17OI bacterial expression vector using the Gateway® technology (Invitrogen, Carlsbad, CA, USA). This vector allows the expression of the recombinant protein under the control of the T7 promoter. The resulting protein is preceded by a stretch of 22 vector-encoded residues (MSYYHHHHHHLESTS LYKKAGF) encompassing a hexahistidine tag.

All constructs were verified by DNA sequencing (Genewiz, Azenta Life Sciences, Leipzig, Germany) and were found to conform to expectations.

4.3 | Proteins expression and purification

The *E. coli* strain T7pRos was used to express all recombinant proteins upon transformation of bacterial cells with each of the bacterial expression plasmids described above. Cultures were grown overnight to saturation in TB medium containing 100 μg/mL ampicillin and 34 μg/mL chloramphenicol. An aliquot of the overnight culture was diluted 1/20 into 1 L of TB medium and grown at 37°C with shaking at 200 rpm. When the optical density at 600 nm (OD_{600}) reached 0.6–0.8, isopropyl β-D-thiogalactopyanoside (IPTG) was added to a final concentration of 1 mM, and the cells were grown at 25°C overnight. The induced cells were harvested, washed and collected by centrifugation (6000 × *g*, 15 min). The resulting pellets were resuspended in 50 mL/L of culture of buffer A (HEPES buffer saline, HBS: 20 mM HEPES, 150 mM NaCl, pH 7.4) containing 6 M urea and then frozen at −20°C. Samples were thawed and sonicated to disrupt the cells (using a 750 W Sonic Vibra-Cell sonicator and cycles of 3 s followed by 1 s of pause each up to a total of 7 min at 80% power output) and then centrifuged at 15,000 × *g* for 30 min at 10°C. The supernatant was first purified by IMAC using 1 mL of nickel resin (Cytiva, Marlborough, MA, USA) pre-equilibrated in buffer A per liter of culture. The affinity resin was washed with 10 column volumes (CV) of buffer A containing 6 M urea and 1 M NaCl, and then with 10 CVs of buffer A containing 6 M urea and 10 mM imidazole. Proteins were eluted with ~8 CV of buffer A, supplemented with 6 M urea and 500 mM imidazole. The eluted fractions were pooled and concentrated in the presence of 6 M urea up to 1 mM using Centricon concentrators (Amicon Ultra-15, MWCO 3 kDa, Millipore, for truncated variants, and Amicon Ultra-15, MWCO 10 kDa, Millipore, for full-length variants), and then frozen at −20°C. All PNT3 variants were subsequently subjected to SEC (Hiload Superdex 75 prep grade column, Cytiva, Marlborough, MA, USA) using buffer A supplemented with 6 M urea as the elution buffer. The SEC fractions were pooled, concentrated (up to ~750 μM), and stored at −20°C. IMAC and SEC were performed at room temperature.

Prior to all subsequent analyses, urea was removed from the protein samples and the buffer was exchanged using Sephadex G-25 medium columns (Cytiva, Marlborough, MA, USA).

Protein concentrations were estimated using the theoretical absorption coefficients at 280 nm as obtained using the program ProtParam from the EXPASY server (http://web.expasy.org/protparam/, Accessed 20 January 2023).

4.4 | Mass spectrometry analyses

The identity of all purified PNT3 variants was confirmed by mass spectrometry analysis of fragments obtained after trypsin or AspN (PNT3 high-κ variant) digestion of the purified protein bands excised from SDS-polyacrylamide gels. The excised bands underwent mass spectrometry analysis by the facility of Marseille Proteomics, as previously described (Nilsson et al., 2022; Salladini et al., 2021).

4.5 | Far-UV circular dichroism

Samples in buffer A containing 6 M urea were buffer exchanged to remove urea and then incubated at 37°C for 3 or 7 days for the PNT3tr and PNT3 variants, respectively. Buffer was exchanged to 10 mM sodium phosphate pH 7.2 immediately prior to CD measurements. The CD spectra were acquired using a nitrogen-

flushed Jasco 810 dichrograph (Jasco France, Lisses, France). Proteins were loaded into a 1-mm quartz cuvette at 10 μM (PNT3 variants) or 20 μM (PNT3tr variants). The scanning speed was 100 nm/min, with a data pitch of 0.2 nm and a bandwidth of 2 nm. Each spectrum represents the average of 10 acquisitions. The spectrum of the buffer was subtracted from the protein spectrum.

Mean molar ellipticity values per residue (MRE) were calculated as

$$[\theta] = 3300 \times m \times \Delta A/(l \times c \times n), \quad (1)$$

where l is the path length (cm), n is the number of residues, m is the molecular mass in Daltons, and c is the concentration of the protein in mg/mL. The numbers of residues were 77 and 133 for the truncated and full-length variants, respectively. The molecular mass is 15,198 Da for all three full-length PNT3 variants. The molecular masses of the PNT3 truncated variants are: 9020 Da for PNT3tr, 8936 Da for PNT3 $R^{all}K$, 9076 Da for PNT3 $K^{all}R$, 9188 Da for PNT3 $G^{all}V$, and 8599 Da for PNT3 $VIL^{all}G$.

The secondary structure content was determined by deconvolution using the Dichroweb server (Whitmore & Wallace, 2004, 2008). The CDSSTR deconvolution algorithm was used for this purpose with the reference protein dataset 7.

4.6 | Estimation of the hydrodynamic radius by SEC

The hydrodynamic radii (Stokes radii, R_S) of the proteins were estimated by analytical SEC using a Superdex 75 Increase 10/300 GL column (Cytiva, Marlborough, MA, USA). Buffer A was used as elution buffer. Typically, 250 μL of purified protein at 2.0 mg/mL in buffer A containing 6 M urea were injected.

The Stokes radii of proteins eluted from the SEC column were deduced from a calibration curve obtained using globular proteins of known molecular mass (MM) (conalbumin: 75 kDa, ovalbumin: 43 kDa, carbonic anhydrase: 29 kDa, RNAse A: 13.7 kDa, aprotinin: 6.5 kDa). The respective R_S values were derived using Equation (2).

The R_S (Å) of a natively folded (Rs^{NF}), fully unfolded state in urea (R_S^U), and natively unfolded premolten globule (PMG) (R_S^{PMG}) protein with molecular mass MM (Daltons) were calculated according to Uversky (2002):

$$\log\left(R_S^{NF}\right) = 0.357 \times (\log \mathrm{MM}) - 0.204 \quad (2)$$

$$\log\left(R_S^{U}\right) = 0.521 \times (\log \mathrm{MM}) - 0.649 \quad (3)$$

$$\log\left(R_S^{PMG}\right) = 0.403 \times (\log \mathrm{MM}) - 0.239 \quad (4)$$

The R_S (Å) of an IDP with N residues was also calculated according to Marsh and Forman-Kay (2010) using the simple power–law model:

$$R_S^{IDP} = R_0 N^{\nu} \quad (5)$$

where $R_0 = 2.49$ and $\nu = 0.509$. The compaction index (CI) is expressed according to Brocca et al. (2011):

$$\mathrm{CI} = \left(R_S^{U} - R_S^{OBS}\right)/\left(R_S^{U} - R_S^{NF}\right) \quad (6)$$

This parameter, which allows comparison between proteins of different lengths, varies between 0 and 1, with 0 indicating minimal compaction and 1 maximal compaction.

4.7 | Turbidity and fluorescence measurements

Protein samples were buffer-exchanged to remove urea before turbidity and fluorescence analyses. Protein samples (100 μM) in buffer A were incubated at 37°C for various times in the presence of 100 μM thioflavin T (ThT, Sigma Aldrich, St. Louis, MO, USA). Turbidity and fluorescence measurements were performed on a Tecan microplate reader GENios Plus in black 96-well plates with a transparent flat bottom (Greiner, 655,096). ThT was excited at 440 nm (slitwidth: 5 nm) and fluorescence emission was recorded at 535 nm (slit width: 10 nm). As a control, the fluorescence of a sample containing only ThT was monitored. All statistical analyses were performed with Prism using Student's *t*-test.

4.8 | Negative-staining transmission electron microscopy

Following buffer exchange to remove urea, all variants, at a concentration of 100 μM, were prepared and analyzed immediately (day 0) and after either 1 or 2 or 3 days (PNT3tr variants) or 1, 2, 3 and 7 days of incubation (PNT3 variants). Incubation was carried out at 37°C in buffer A supplemented with 100 μM ThT. EM grids (carbon-coated copper grids, 300 mesh, Agar Scientific, UK) were exposed to plasma glow discharge for 30 s using GloQube (Quorum, UK) (current 15 mA) in order to increase protein adhesion. Drops of 3.5 μL of protein solutions at a concentration of 2 μM were deposited onto glow-discharged grids. After 1 min incubation, the grids were washed three times with 50 μL of

buffer A, once with 35 μL of 1% (w/v) uranyl acetate solution (Laurylab, Brindas, France), and then stained for 1 min in the latter solution. Excess uranyl was blotted, and the grids were left to dry for 1 h at RT. Images were collected using a Tecnai 120 Spirit TEM microscope (FEI company, Thermo Fisher, Illkirch-Graffenstaden, France) operated at 120 kV using a Veleta 2Kx2K CCD camera (Olympus).

4.9 | Raman spectroscopy

All the Raman spectra were acquired using an InVia laser Raman microscope (Renishaw, UK). After removal of urea, samples, containing 100 μM protein in Buffer A in a final volume of 500 μL, were incubated at 37°C for either 1 day (PNT3tr $R^{all}K$) or 3 days (PNT3tr). The reaction mixtures were subsequently subjected to high-speed centrifugation at 16,400 rpm for 60 min. After careful removal of the supernatant without disturbing the pellet, the pelleted fibrils were resuspended in 10 μL of sodium phosphate buffer (20 mM sodium phosphate, pH 7.5), deposited onto a glass slide covered with aluminium foil, and allowed to air dry. The half-dried samples were focused using a 100× objective lens (Nikon, Japan) and excited with a 785 nm near-infrared (NIR) laser with a 10 s exposure time at full laser power (500 mW). Rayleigh scattering was blocked using an edge filter, whereas Raman scattering was dispersed using a 1200 lines/mm diffraction grating and detected with an air-cooled CCD detector. Raman measurements were repeated at least three times using fibrils prepared from different batches of protein. Data acquisition was performed using built-in Wire 3.4 software, averaging 10 accumulations for each spectrum. Baseline correction of each spectrum was performed using the cubic spline interpolation method, followed by smoothing using the Wire 3.4 software. The spectra were normalized and plotted using the Origin 2021b software. To obtain fitted Gaussian curves, amide band fitting was performed using the Levenberg-Marquadt non-linear least-squares method in Origin 2021b.

4.10 | Small-angle X-ray scattering

To ensure maximal monodispersity of the samples, SAXS studies were coupled with SEC. SEC-SAXS data for PNT3 low-κ were collected at SOLEIL (Gif-sur-Yvette, France), while data for PNT3 and PNT3 high-κ were collected at the ESRF (Grenoble, France), as described in Table 4. Data reduction and frame subtraction were performed using the beamline software FOXTROT (available upon request from SOLEIL staff). Whenever necessary, gaussian decomposition was performed using the UltraScan solution modeler

TABLE 4 SEC-SAXS data acquisition parameters.

Instrument	ESRF synchrotron (Grenoble, France) beamline BM29	SOLEIL synchrotron (Gif-sur-Yvette, France) beamline swing
X-ray wavelength (Å)	1.0	1.033
Energy (keV)	12.5	12
Detector type	Pilatus3 2M	Dectris EIGER 4M
Sample-to-detector distance (m)	2.867	2.0
q-Range	0.063–5.209 nm^{-1}	0.003–0.549 $Å^{-1}$
Temperature (°C)	20	20
Samples		
Concentration (mg/mL)	7	7
Sample volume (μL)	45	50
Gel filtration column	Biosec 3-300 (Agilent)	Biosec 3-300 (Agilent)
Flow rate (mL/min)	0.3	0.3
Buffer	A	A

(US-SOMO) HPLC-SAXS module (https://somo.aucsolutions.com/) (Brookes & Rocco, 2018). Otherwise, Chromixs was employed to manually select frames (Panjkovich & Svergun, 2018) and the final deconvoluted scattering curves were submitted to the SHANUM program (Manalastas-Cantos et al., 2021) to remove noisy and non-informative data at high angles.

Data were analyzed using the ATSAS program package (Manalastas-Cantos et al., 2021). The radius of gyration (R_g) and $I(0)$ were estimated at low angles ($q.R_g < 1.1$) according to the Guinier approximation (Guinier, 1939; Guinier & Fournet, 1955):

$$\mathrm{Ln}[I(q)] = \mathrm{Ln}[I_0] - \left(q^2 {R_g}^2\right)/3 \quad (7)$$

The pairwise distance distribution functions $P(r)$, from which D_{max} and R_g were estimated, were calculated using the program GNOM (Svergun, 1992) and manually adjusted until a good CorMap p-value ($\alpha > 0.01$) was obtained (Svergun, 1992).

The theoretical R_g value (Å) expected for various conformational states was calculated using Flory's equation:

$$R_g = R_0 N^{\nu} \quad (8)$$

where N is the number of amino acid residues, R_0 is a constant, and ν is the scaling factor. For IDPs, R_0 is 2.54 ± 0.01 and ν is 0.522 ± 0.01 (Bernado & Blackledge, 2009), for chemically denatured (U) proteins R_0 is 1.927 ± 0.27 and ν is 0.598 ± 0.028

(Bernado & Blackledge, 2009), and for natively folded (NF) proteins $R_0 = \sqrt{(3/5)} \times 4.75$ and $\nu = 0.29$ (Wilkins et al., 1999).

The overall conformation and flexibility of the proteins were assessed using the dimensionless Kratky plot ($(qR_g)^2\ I(q)/I_0$ vs. qR_g). The online version of the Ensemble Optimization Method 3.0 (EOM) was employed (Bernado et al., 2007; Tria et al., 2015) to deconvolute the scattering intensities. Default parameters were used, except for the number of harmonics, which was set to 99.

SEC-SAXS data have been deposited in the Small Angle Scattering Biological Data Bank (SASBDB) (Valentini et al., 2015) under the following codes: SASDVC8 (PNT3), SASDVD8 (PNT3 low-κ), and SASDVE8 (PNT3 high-κ).

AUTHOR CONTRIBUTIONS

Frank Gondelaud: Investigation; writing – original draft; writing – review and editing; conceptualization; formal analysis; project administration; validation. **Julien Leval:** Investigation. **Lisha Arora:** Investigation; writing – review and editing; formal analysis; validation. **Anuja Walimbe:** Writing – review and editing; investigation; formal analysis; validation. **Christophe Bignon:** Investigation; writing – review and editing. **Denis Ptchelkine:** Writing – review and editing; investigation. **Stefania Brocca:** Writing – review and editing; conceptualization. **Samrat Mukhopadyay:** Funding acquisition; writing – review and editing; conceptualization; validation. **Sonia Longhi:** Conceptualization; funding acquisition; writing – original draft; writing – review and editing; supervision; project administration; validation.

ACKNOWLEDGMENTS

We thank Aurélien Thureau (SOLEIL) and Petra Pernot (ESRF) for their help in recording the SEC-SAXS data and both synchrotrons for beamtime allocation (SOLEIL BAG project 20181038). We are also grateful to Gerlind Sulzenbacher (AFMB Lab) for efficiently managing AFMB BAG. We thank all the AFMB technical and support staff (Denis Patrat, Patricia Clamecy, Béatrice Rolland, Chantal Falaschi and Fabienne Amalfitano). We thank the mass spectrometry facility of Marseille Proteomics (marseille-proteomique.univ-amu.fr), supported by IBISA (Infrastructures Biologie Santé et Agronomie), Plateforme Technologique Aix-Marseille, the Cancéropôle PACA, Région Sud-Alpes-Côte d'Azur, the Institut Paoli-Calmettes, the Centre de Recherche en Cancérologie de Marseille (CRCM), Fonds Européen de Développement Régional and Plan Cancer. This work was carried out with the financial support of the Agence Nationale de la Recherche (ANR), specific project Heniphase (ANR-21-CE11-0012-01) and of the Centre Franco-Indien pour la Promotion de la Recherche Avancée (CEFIPRA), specific Collaborative Scientific Research Programme (CSRP) No. 6903-3 to S.L. This study was also partly supported by the French Infrastructure for Integrated Structural Biology (FRISBI) (ANR-10-INSB-0005) and CNRS. F.G. was supported by a post-doctoral fellowship from the FRM (Fondation pour la Recherche Médicale) and by the FRM specific project MND202310017898. We thank the Indo-French Centre for the Promotion of Advanced Research (IFC/A/6903-3/2023/680 to S.M.), the Science and Engineering Research Board (J.C. Bose Fellowship JCB/2023/000016 to S.M.), and the Ministry of Education, Govt. of India (Prime Minister's Research Fellowship to A.W.) for financial support. The funders had no role in the design of the study; in the collection, analyses, or interpretation of data; in the writing of the manuscript, or in the decision to publish the results. A CC-BY public copyright license has been applied by the authors to the present document and will be applied to all subsequent versions up to the Author Accepted Manuscript arising from this submission, in accordance with the grant open access conditions.

DATA AVAILABILITY STATEMENT

The data that support the findings of this study are available from the corresponding author upon reasonable request.

ORCID

Samrat Mukhopadyay https://orcid.org/0000-0003-1242-9958
Sonia Longhi https://orcid.org/0000-0002-6829-6771

REFERENCES

Abdella R, Aggarwal M, Okura T, Lamb RA, He Y. Structure of a paramyxovirus polymerase complex reveals a unique methyltransferase-CTD conformation. Proc Natl Acad Sci U S A. 2020;117:4931–41.

Audsley MD, Moseley GW. Paramyxovirus evasion of innate immunity: diverse strategies for common targets. World J Virol. 2013; 2:57–70.

Avni A, Joshi A, Mukhopadhyay S. Hydrogen–deuterium exchange vibrational Raman spectroscopy distinguishes distinct amyloid polymorphs comprising altered core architecture. J Phys Chem Lett. 2023;14:5592–601.

Beltrandi M, Blocquel D, Erales J, Barbier P, Cavalli A, Longhi S. Insights into the coiled-coil organization of the Hendra virus phosphoprotein from combined biochemical and SAXS studies. Virology. 2015;477:42–55.

Bernado P, Blackledge M. A self-consistent description of the conformational behavior of chemically denatured proteins from NMR and small angle scattering. Biophys J. 2009;97:2839–45.

Bernado P, Mylonas E, Petoukhov MV, Blackledge M, Svergun DI. Structural characterization of flexible proteins using small-angle X-ray scattering. J Am Chem Soc. 2007;129:5656–64.

Bianchi G, Mangiagalli M, Barbiroli A, Longhi S, Grandori R, Santambrogio C, et al. Distribution of charged residues affects the average size and shape of intrinsically disordered proteins. Biomolecules. 2022;12:561.

Bianchi G, Mangiagalli M, Ami D, Ahmed J, Lombardi S, Longhi S, et al. Condensation of the N-terminal domain of human topoisomerase 1 is driven by electrostatic interactions and tuned by its charge distribution. Int J Biol Macromol. 2024;254:127754.

Whitmore L, Wallace BA. Protein secondary structure analyses from circular dichroism spectroscopy: methods and reference databases. Biopolymers. 2008;89:392–400.
Blocquel D, Habchi J, Gruet A, Blangy S, Longhi S. Compaction and binding properties of the intrinsically disordered C-terminal domain of Henipavirus nucleoprotein as unveiled by deletion studies. Mol Biosyst. 2012;8:392–410.
Blocquel D, Beltrandi M, Erales J, Barbier P, Longhi S. Biochemical and structural studies of the oligomerization domain of the Nipah virus phosphoprotein: evidence for an elongated coiled-coil homotrimer. Virology. 2013;446:162–72.
Bloyet LM, Welsch J, Enchery F, Mathieu C, de Breyne S, Horvat B, et al. HSP90 chaperoning in addition to phosphoprotein required for folding but not for supporting enzymatic activities of measles and Nipah virus L polymerases. J Virol. 2016;90:6642–56.
Bloyet LM, Schramm A, Lazert C, Raynal B, Hologne M, Walker O, et al. Regulation of measles virus gene expression by P protein coiled-coil properties. Sci Adv. 2019;5:eaaw3702.
Brocca S, Testa L, Sobott F, Samalikova M, Natalello A, Papaleo E, et al. Compaction properties of an intrinsically disordered protein: sic1 and its kinase-inhibitor domain. Biophys J. 2011;100:2243–52.
Brookes E, Rocco M. Recent advances in the ultrascan solution modeller (US-SOMO) hydrodynamic and small-angle scattering data analysis and simulation suite. Eur Biophys J. 2018;47:855–64.
Bruhn-Johannsen JF, Barnett K, Bibby J, Thomas J, Keegan R, Rigden D, et al. Crystal structure of the Nipah virus phosphoprotein tetramerization domain. J Virol. 2014;88:758–62.
Cloe AL, Orgel JP, Sachleben JR, Tycko R, Meredith SC. The Japanese mutant Aβ (ΔE22-Aβ(1-39)) forms fibrils instantaneously, with low-thioflavin T fluorescence: seeding of wild-type Aβ(1-40) into atypical fibrils by ΔE22-Aβ(1-39). Biochemistry. 2011;50:2026–39.
Communie G, Habchi J, Yabukarski F, Blocquel D, Schneider R, Tarbouriech N, et al. Atomic resolution description of the interaction between the nucleoprotein and phosphoprotein of Hendra virus. PLoS Pathog. 2013;9:e1003631.
Das RK, Pappu RV. Conformations of intrinsically disordered proteins are influenced by linear sequence distributions of oppositely charged residues. Proc Natl Acad Sci U S A. 2013;110:13392–7.
Devitt G, Rice W, Crisford A, Nandhakumar I, Mudher A, Mahajan S. Conformational evolution of molecular signatures during amyloidogenic protein aggregation. ACS Chem Nerosci. 2019;10:4593–611.
Douglas J, Drummond AJ, Kingston RL. Evolutionary history of cotranscriptional editing in the paramyxoviral phosphoprotein gene. Virus Evol. 2021;7(1):veab028. https://doi.org/10.1093/ve/veab028
Eaton BT, Broder CC, Middleton D, Wang LF. Hendra and Nipah viruses: different and dangerous. Nat Rev Microbiol. 2006;4:23–35.
Eaton BT, Mackenzie JS, Wang LF. Henipaviruses. In: Fields BN, Knipe DM, Howley PM, editors. Fields virology. Philadelphia: Lippincott-Raven; 2007. p. 1587–600.
Fontana JM, Bankamp B, Rota PA. Inhibition of interferon induction and signaling by paramyxoviruses. Immunol Rev. 2008;225:46–67.
Gallivan JP, Dougherty DA. Cation–pi interactions in structural biology. Proc Natl Acad Sci U S A. 1999;96:9459–64.
Garaizar A, Sanchez-Burgos I, Collepardo-Guevara R, Espinosa JR. Expansion of intrinsically disordered proteins increases the range of stability of liquid–liquid phase separation. Molecules. 2020;25:4705.
Garbuzynskiy SO, Lobanov MY, Galzitskaya OV. FoldAmyloid: a method of prediction of amyloidogenic regions from protein sequence. Bioinformatics. 2010;26:326–32.
Gondelaud F, Pesce G, Nilsson JF, Bignon C, Ptchelkine D, Gerlier D, et al. Functional benefit of structural disorder for the replication of measles, Nipah and Hendra viruses. Essays Biochem. 2022;66:915–34.
Gondelaud F, Lalande A, Pesce G, Bignon C, Fourquet P, Ptchelkine D, et al. Redox-dependent formation of a viral amyloid and functional impact. bioRxiv. 2024. https://doi.org/10.1101/2024.01.22.576663
Gruet A, Longhi S, Bignon C. One-step generation of error-prone PCR libraries using gateway® technology. Microb Cell Fact. 2012;11:14.
Guinier A. La diffraction des rayons X aux tres petits angles; application a l'etude de phenomenes ultramicroscopiques. Ann Phys Paris. 1939;12:161–237.
Guinier A, Fournet F. Small angle scattering of X-rays. New York: Wiley Interscience; 1955.
Habchi J, Mamelli L, Darbon H, Longhi S. Structural disorder within Henipavirus nucleoprotein and phosphoprotein: from predictions to experimental assessment. PLoS One. 2010;5:e11684.
Habchi J, Blangy S, Mamelli L, Jensen MR, Blackledge M, Darbon H, et al. Characterization of the interactions between the nucleoprotein and the phosphoprotein of Henipavirus. J Biol Chem. 2011;286:13583–602.
Hernández B, Coïc YM, Pfluger F, Kruglik S, Ghomi M. All characteristic Raman markers of tyrosine and tyrosinate originate from phenol ring fundamental vibrations. J Raman Spectrosc. 2015;47:212–20.
Holehouse AS, Das RK, Ahad JN, Richardson MO, Pappu RV. CIDER: resources to analyze sequence-ensemble relationships of intrinsically disordered proteins. Biophys J. 2017;112:16–21.
Jensen MR, Yabukarski F, Communie G, Condamine E, Mas C, Volchkova V, et al. Structural description of the Nipah virus phosphoprotein and its interaction with STAT1. Biophys J. 2020;118:2470–88.
Ker DS, Jenkins HT, Greive SJ, Antson AA. CryoEM structure of the Nipah virus nucleocapsid assembly. PLoS Pathog. 2021;17:e1009740.
Kumar K, Woo SM, Siu T, Cortopassi WA, Duarte F, Paton RS. Cation–π interactions in protein–ligand binding: theory and data-mining reveal different roles for lysine and arginine. Chem Sci. 2018;9:2655–65.
Liang Q, Peng N, Xie Y, Kumar N, Gao W, Miao Y. MolPhase, an advanced prediction algorithm for protein phase separation. EMBO J. 2024;43:1898–918.
Lieutaud P, Canard B, Longhi S. MeDor: a metaserver for predicting protein disorder. BMC Genomics. 2008;9:S25.
Maiti NC, Apetri MM, Zagorski MG, Carey PR, Anderson VE. Raman spectroscopic characterization of secondary structure in natively unfolded proteins: alpha-synuclein. J Am Chem Soc. 2004;126:2399–408.
Maltseva D, Chatterjee S, Yu CC, Brzezinski M, Nagata Y, Gonella G, et al. Fibril formation and ordering of disordered FUS LC driven by hydrophobic interactions. Nat Chem. 2023;15:1146–54.
Manalastas-Cantos K, Konarev PV, Hajizadeh NR, Kikhney AG, Petoukhov MV, Molodenskiy DS, et al. ATSAS 3.0: expanded functionality and new tools for small-angle scattering data analysis. J Appl Cryst. 2021;54:343–55.
Marsh JA, Forman-Kay JD. Sequence determinants of compaction in intrinsically disordered proteins. Biophys J. 2010;98:2383–90.
Martinho M, Habchi J, El Habre Z, Nesme L, Guigliarelli B, Belle V, et al. Assessing induced folding within the intrinsically disordered C-terminal domain of the Henipavirus nucleoproteins by site directed spin labeling EPR spectroscopy. J Biomol Struct Dyn. 2013;31:453–71.
Nilsson JF, Baroudi H, Gondelaud F, Pesce G, Bignon C, Ptchelkine D, et al. Molecular determinants of fibrillation in a viral

amyloidogenic domain from combined biochemical and biophysical studies. Int J Mol Sci. 2022;24:399.
Nomura T, Watanabe S, Kaneko K, Yamanaka K, Nukina N, Furukawa Y. Intranuclear aggregation of mutant FUS/TLS as a molecular pathomechanism of amyotrophic lateral sclerosis. J Biol Chem. 2014;289:1192–202.
Nott TJ, Petsalaki E, Farber P, Jervis D, Fussner E, Plochowietz A, et al. Phase transition of a disordered nuage protein generates environmentally responsive membraneless organelles. Mol Cell. 2015;57:936–47.
Pak CW, Kosno M, Holehouse AS, Padrick SB, Mittal A, Ali R, et al. Sequence determinants of intracellular phase separation by complex coacervation of a disordered protein. Mol Cell. 2016;63:72–85.
Panjkovich A, Svergun DI. CHROMIXS: automatic and interactive analysis of chromatography-coupled small-angle X-ray scattering data. Bioinformatics. 2018;34:1944–6.
Pesce G, Gondelaud F, Ptchelkine D, Nilsson JF, Bignon C, Cartalas J, et al. Experimental evidence of intrinsic disorder and amyloid formation by the Henipavirus W proteins. Int J Mol Sci. 2022;23:923.
Pesce G, Gondelaud F, Ptchelkine D, Bignon C, Fourquet P, Longhi S. Dissecting Henipavirus W proteins conformational and fibrillation properties: contribution of their N- and C-terminal constituent domains. FEBS J. 2025;292:556–81.
Rygula A, Majzner K, Marzec KM, Kaczor A, Pilarczyk M, Baranska M. Raman spectroscopy of proteins: a review. J Raman Spectrosc. 2013;44:1061–76.
Salladini E, Delauzun V, Longhi S. The Henipavirus V protein is a prevalently unfolded protein with a zinc-finger domain involved in binding to DDB1. Mol Biosyst. 2017;13:2254–67.
Salladini E, Gondelaud F, Nilsson J, Pesce G, Bignon C, Murrali MG, et al. Identification of a region in the common amino-terminal domain of Hendra virus P, V and W proteins responsible for phase transition and amyloid formation. Biomolecules. 2021;11:1324.
Schiavina M, Salladini E, Murrali MG, Tria G, Felli IC, Pierattelli R, et al. Ensemble description of the intrinsically disordered N-terminal domain of the Nipah virus P/V protein from combined NMR and SAXS. Sci Rep. 2020;10:19574.
Schramm A, Bignon C, Brocca S, Grandori R, Santambrogio C, Longhi S. An arsenal of methods for the experimental characterization of intrinsically disordered proteins—how to choose and combine them? Arch Biochem Biophys. 2019;676:108055.
Schuster BS, Dignon GL, Tang WS, Kelley FM, Ranganath AK, Jahnke CN, et al. Identifying sequence perturbations to an intrinsically disordered protein that determine its phase-separation behavior. Proc Natl Acad Sci U S A. 2020;117:11421–31.
Siamwiza MN, Lord RC, Chen MC, Takamatsu T, Harada I, Matsuura H, et al. Interpretation of the doublet at 850 and 830 cm^{-1} in the Raman spectra of tyrosyl residues in proteins and certain model compounds. Biochemistry. 1975;14:4870–6.
Sulatskaya AI, Rychkov GN, Sulatsky MI, Rodina NP, Kuznetsova IM, Turoverov KK. Thioflavin T interaction with acetylcholinesterase: new evidence of 1:1 binding stoichiometry obtained with samples prepared by equilibrium microdialysis. ACS Chem Nerosci. 2018;9:1793–801.
Svergun D. Determination of the regularization parameters in indirect-transform methods using perceptual criteria. J Appl Cryst. 1992;25:495–503.
Tedeschi G, Salladini E, Santambrogio C, Grandori R, Longhi S, Brocca S. Conformational response to charge clustering in synthetic intrinsically disordered proteins. Biochim Biophys Acta Gen Subj. 2018;1862:2204–14.
Tria G, Mertens HDT, Kachala M, Svergun D. Advanced ensemble modelling of flexible macromolecules using X-ray solution scattering. IUCrJ. 2015;2:202–17.
Tsimbalyuk S, Cross EM, Hoad M, Donnelly CM, Roby JA, Forwood JK. The intrinsically disordered W protein is multifunctional during Henipavirus infection, disrupting host signalling pathways and nuclear import. Cells. 2020;9:1913.
Tuma R. Raman spectroscopy of proteins: from peptides to large assemblies. J Raman Spectrosc. 2005;36:307–19.
Uversky VN. Natively unfolded proteins: a point where biology waits for physics. Protein Sci. 2002;11:739–56.
Valentini E, Kikhney AG, Previtali G, Jeffries CM, Svergun DI. SASBDB, a repository for biological small-angle scattering data. Nucleic Acids Res. 2015;43:D357–63.
Whitmore L, Wallace BA. DICHROWEB, an online server for protein secondary structure analyses from circular dichroism spectroscopic data. Nucleic Acids Res. 2004;32:W668–73.
Wilkins DK, Grimshaw SB, Receveur V, Dobson CM, Jones JA, Smith LJ. Hydrodynamic radii of native and denatured proteins measured by pulse field gradient NMR techniques. Biochemistry. 1999;38:16424–31.

SUPPORTING INFORMATION

Additional supporting information can be found online in the Supporting Information section at the end of this article.

How to cite this article: Gondelaud F, Leval J, Arora L, Walimbe A, Bignon C, Ptchelkine D, et al. Unraveling the molecular grammar and the structural transitions underlying the fibrillation of a viral fibrillogenic domain. Protein Science. 2025; 34(3):e70068. https://doi.org/10.1002/pro.70068